Supplementary Information

Rapid in situ bulk transformation of NiFe particle for highly efficient oxygen evolution in anion exchange membrane water electrolyzers

Bin Chen[a,‡], Fan Bai[b,‡], Yingjie Feng[b*], Sipu Wang[a], Xinyi Cao[a], Wei Li[b], Lianqin Wang [a, c], Xiaoyue Fu[b], Li Jin[b], Junfeng Zhang[a, c, *], Yan Yin[a, c, *] and Michael D. Guiver [a, c]

[a] State Key Laboratory of Engines, School of Mechanical Engineering, Tianjin University, Tianjin, 300350, China

[b] SINOPEC (Beijing) Research Institute of Chemical Industry Co., Ltd., Beijing 100013, China

[c] National Industry-Education Platform of Energy Storage, Tianjin University, Tianjin 300072, Tianjin, China.

*Corresponding author. E-mail geosign@tju.edu.cn; fengyj.bjhy@sinopec.com; yanyin@tju.edu.cn

‡These authors contributed equally to this work

■ Characterization of materials

To observe the morphology of the samples, scanning electron microscopy (SEM) images were collected with an operating voltage of 3 kV on a S4800 or Regulus8100. Raman spectra were collected using a confocal microscope (Horiba LabRAM HR Evolution) with an excitation wavelength of 523 nm. Field-emission transmission electron microscope (FE-TEM) images were obtained on a JSM-2100F FE-TEM (JEOL) instrument, and the distribution of Ni, Fe and Mo elements was obtained by an energy-dispersive X-ray detector (EDX) attached to an FE-TEM. X-ray photoelectron spectral (XPS) patterns were recorded using an X-ray photoelectron spectrometer (Thermo Scientific K-Alpha) with an Al Kα source (1486.6 eV). The elemental composition of the catalyst was analyzed by inductively coupled plasma atomic emission spectroscopy (ICP-OES, Agilent 5800). The Electron paramagnetic resonance (EPR) spectra were conducted by an EPR spectrometer (Bruker EMX PLUSn) at an X-band frequency (around 9.841030 GHz).

■ Electrochemical measurements

The electrochemical OER activity and stability were measured on the Autolab workstation by using a typical three-electrode system in 1 M KOH. One Ag/AgCl, was used as the reference electrode, and a carbon road was used as the counter electrode. The linear sweep voltammetry (LSV) were conducted at a scan rate of 5 mV s^{-1} with *iR*-compensation.

The electrochemical double-layer capacitance (C_{dl}) which can be used to calculate the electrochemically active surface area (ECSA) can be measured by CV scans at the different scan rates (ranging from 20 to 100 mV s^{-1}) in 1 M KOH solution. By plotting the curve of Δj ($\Delta j = (j_{anode} - j_{cathode})/2$) against the scanning rate, the slope of the plots gives C_{dl}. Then, the ECSA values were calculated based on the following equation: ECSA = C_{dl}/C_s, where C_s is the specific capacitance of the sample, and the value of C_s is 0.04 mF cm^{-2} in 1 M KOH based on the typical reported value.

The turnover frequency (TOF) was calculated as follows:

$$TOF = j/4nF \quad \text{(Eq. S1)}$$

where j is the current during the linear sweep measurement (A), F is Faraday's constant (96485 C mol^{-1}), n is the number of moles of metal on the electrode, which was measured by ICP-mass spectrometry. It is assumed that all Ni, Fe and Mo atoms are active and contribute to the catalytic reaction (the minimum values of TOF are

calculated).

■ In Situ Raman Spectroscopy

A Horiba Labram HR Evolution Raman instrument with 532 nm excitation was carried out for the in situ Raman spectroscopy. In situ Raman spectroscopy was tested in a home-built electrochemical cell with Ag/AgCl and platinum foil as reference and counter electrodes, respectively. To prepare the working electrode, the electrocatalyst ink was sprayed onto carbon paper as the working electrode. Before the test, 20 cycles of CV were used to activate the working electrode. Then, the electrode was kept at the desired potential for 5 minutes to collect the steady-state spectrum.

■ Computation details

All the DFT calculations were carried out using the spin-polarized density functional theory with periodic boundary conditions in the CASTEP program.[1] The generalized gradient approximation (GGA) of revised Perdew–Burke–Ernzerhof (RPBE) was employed for the electronic exchange-correlation potential. The Hubbard *U* term was added to improve the description of transition metal ions in OER process.[2] The corresponding *U* values for Ni, Fe and Mo are 4.50 eV, 3.00 eV and 2.00 eV, respectively, similar to values used in previous DFT + *U* studies for transition metal oxyhydroxide.[3,4] The plane wave cut-off energy was chosen to be 571.40 eV and a *k*-point was generated by the Monkhorst–Pack grid method with 2 × 1 × 1.[5] The self-consistent total energy convergence criteria were less than 2×10^{-6} eV, whereas the convergence of geometry optimization was set to following values: (1) energy tolerance: 2×10^{-5} eV per atom; (2) maximum force tolerance: 0.05 eV/Å; (3) maximum displacement tolerance: 2×10^{-3} Å.

In the bulk of NiOOH slab, there are 24 Ni atoms, 48 O atoms and 24 H atoms. There were eight Ni atoms substituted by Fe atoms, and four Fe atoms substituted by Mo atoms in NiFeOOH and Mo-NiFeOOH slab, respectively. Based on the relaxed bulk slabs, the models containing three metal atomic layers with the bottom one layer fixed was established and denoted as $NiFeO_xH_y$ and Mo-$NiFeO_xH_y$, respectively. Vacuum slabs of 15 Å were used to avoid interactions between adjacent atom layers. The V_{Mo}-$NiFeO_xH_y$ slab was constructed by removing one Mo atom from the surface.

For the OER, the Gibbs free energy (ΔG) was calculated based on the following intermediate steps[3]

$$* + H_2O \rightarrow *OH + H^+ + e^- \qquad \text{(Eq. S2)}$$

$$*OH \rightarrow *O + H^+ + e^- \quad \text{(Eq. S3)}$$

$$*O + H_2O \rightarrow *OOH + H^+ + e^- \quad \text{(Eq. S4)}$$

$$*OOH \rightarrow * + O_2 + H^+ + e^- \quad \text{(Eq. S5)}$$

where *, *OH, *O and *OOH represent the clean surface and hydroxyl-, oxo-, and hydroperoxide intermediates adsorbed on the surface. The free energy change of each step involving one electron transfer can be expressed by following equation[6]

$$\Delta G_i = \Delta E_i + \Delta ZPE - T\Delta S - eU - k_B T \ln [H^+] \quad \text{(Eq. S6)}$$

where ΔE_i, ΔZPE, $T\Delta S$ and U are the electronic energy difference in Eq. S2-S5, zero-point energy correction, entropy, and the applied potential during the OER, respectively. The ZPE and the entropic contribution of the relevant species are taken from previous work.[7] Under standard conditions (T = 298 K, pH = 0, p = 1 bar), the G of O_2 is derived from the equation $G[O_2] = 4.92$ eV + $2G[H_2O] - 2G[H_2]$, and the G of $H^+ + e^-$ is obtained as the equation $G[H^+ + e^-] = 1/2\ G[H_2]$ using the computational hydrogen electrode (CHE) approach.[8] For an ideal catalyst, the free energy changes (ΔG_0) of overall OER at the equilibrium potential U_0 should be $\Delta G_0 = \Delta G_1 + \Delta G_2 + \Delta G_3 + \Delta G_4 = 0$. Normally, an additional overpotential is required to drive the step with the largest ΔG_i. The overpotential η is defined by

$$\eta = 1/e \times \max [\Delta G_i] - U_0 \quad \text{(Eq. S7)}$$

■ The assembly of AEMWE

For the anode and cathode, IrO_2 or Mo-NiFe (as-synthesized) catalysts, and Pt/C were ultrasonically dispersed in a mixture of PiperIon-A5-HCO3 ionomer (with a weight ratio of Ionomer/Catalyst = 0.2) and a mixed solvent of isopropanol and water (3:1 v/v) to form a homogeneous catalyst ink. Ni foam (0.5 mm thickness) and carbon paper (TGP-H-060) were used as the gas diffusion layers (GDLs) for the anode and cathode, respectively. The GDLs were subsequently taped to a hot plate maintained at 80 °C, and catalyst inks was sprayed onto the GDL using an airbrush, achieving a loading of ~1.0 mg cm^{-2}. The PiperION-A40R-HCO3 membrane, after being pretreated by immersion in 1 M KOH solution for 12 hours, was assembled with GDLs and Teflon gaskets into a single cell, using a controlled torque of 4 N·m. The cell was tested by a PTC-05100EW electrochemical workstation combination with a DC power supply (IT6723C). Before the test, 20 CV (1.2–2.0 V) was applied to active the cell while flowing 1 M KOH solution on both the anode and cathode at 60 °C until the polarization

curves stabilized. Then, polarization curves were recorded under a scan rate of 10 mV s^{-1}.

■ **Electrochemical activation energy (E_a)**

The electrochemical activation energy (E_a) for AEMWE can be obtained through the Arrhenius relationship:

$$\frac{\partial \log(i)}{\partial \frac{1}{T}} = -\frac{E_a}{2.3R} \quad \text{(Eq. S8)}$$

where i is the current density at 1.8 V_{cell} in this work, T is the temperature in K, and R (8.314 J K^{-1} mol^{-1}) is the gas constant.

■ **Faradaic efficiency of the AEMWE**

The Faradaic efficiency of the AEMWE was calculated by measuring the real hydrogen flow rate and the theoretical hydrogen flow rate at different current densities. The hydrogen flow rate can be measured by a displacement method.

The Faradaic efficiency can be calculated by the following equation.

$$\text{Faradaic efficiency} = \frac{F}{\frac{A\,I\,t}{2e/N_A} \times 24.5} \times 100\% \quad \text{(Eq. S9)}$$

where F (L) is the measured flowrate of the generated hydrogen; A (cm^2) denotes the active area of the membrane electrode assembly; I (A cm^{-2}) is the applied current density during the durability test; t (s) is the operation time during the test; e and N_A are the quantity of electric charge (e = 1.602 × 10^{-19} C) and Avogadro constant (6.02214076 × 10^{23}), respectively. At 25 ℃, the molar volume of gas is about 24.5 L mol^{-1} at 1.01 × 10^5 Pa.

Fig. S1 Optical photos of the precursor, from left to right, show NiFe, $Mo_{0.25}$-NiFe, Mo-NiFe, $Mo_{0.75}$-NiFe, $Mo_{1.0}$-NiFe.

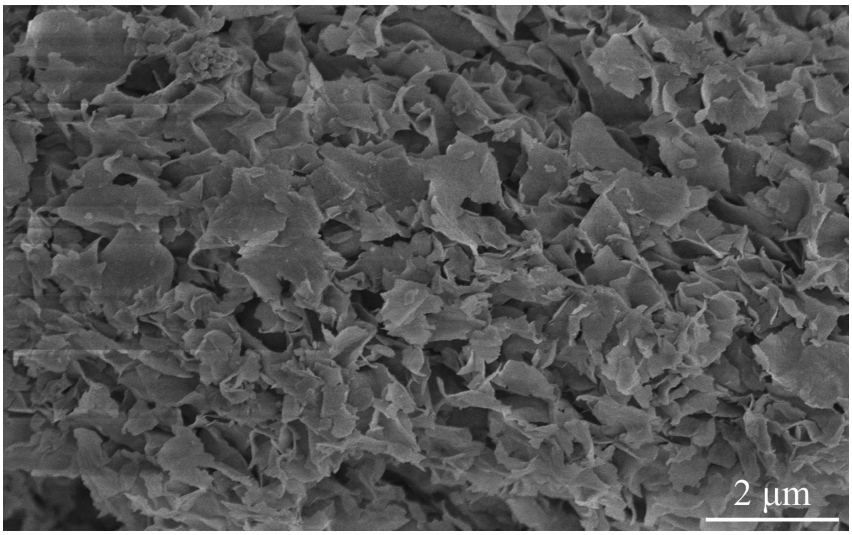

Fig. S2 SEM of Mo-NiFe precursor exhibits a nanosheet morphology.

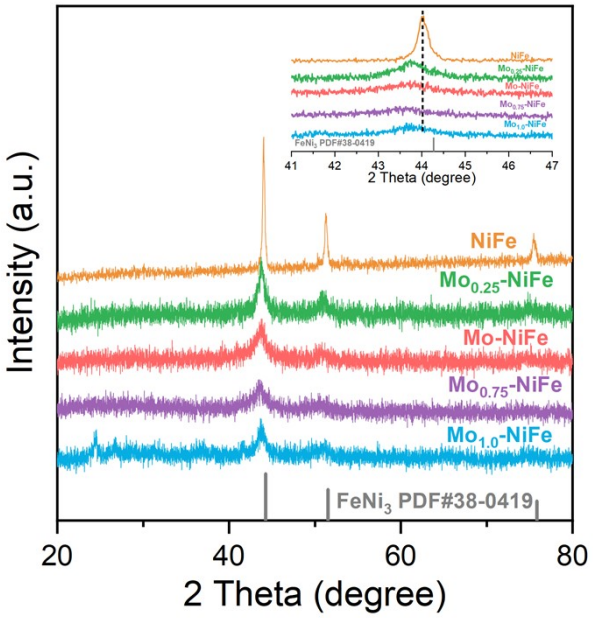

Fig. S3 XRD patterns of NiFe, $Mo_{0.25}$-NiFe, Mo-NiFe, $Mo_{0.75}$-NiFe, $Mo_{1.0}$-NiFe.

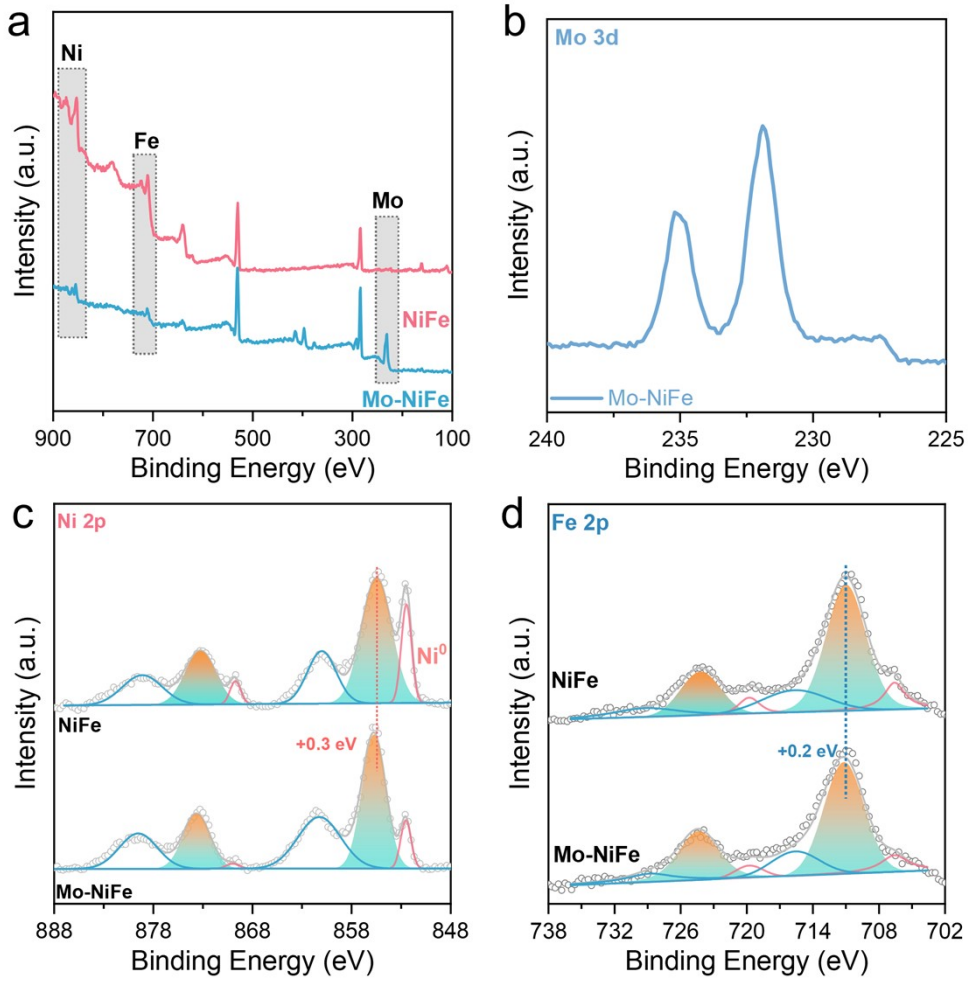

Fig. S4 XPS of NiFe and Mo-NiFe.

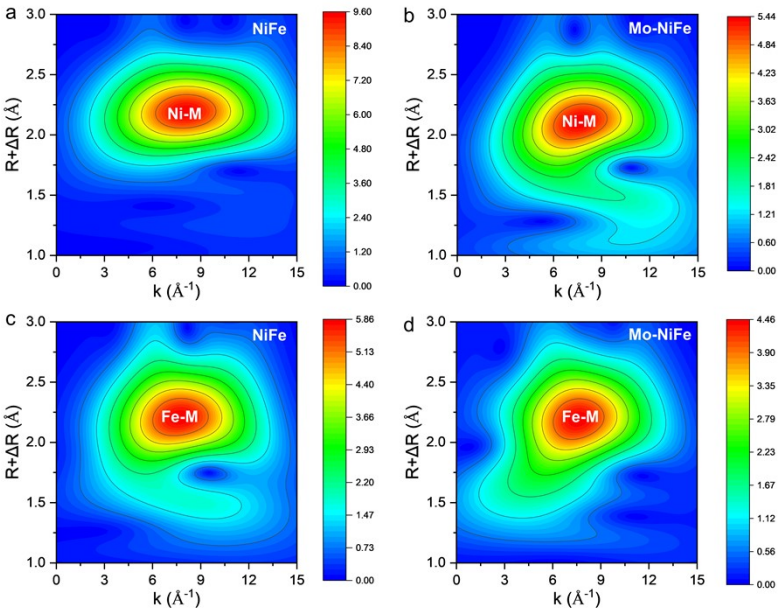

Fig. S5 Wavelet-transform EXAFS spectra of (a-b) Ni and (c-d) Fe K-edge for NiFe and Mo-NiFe.

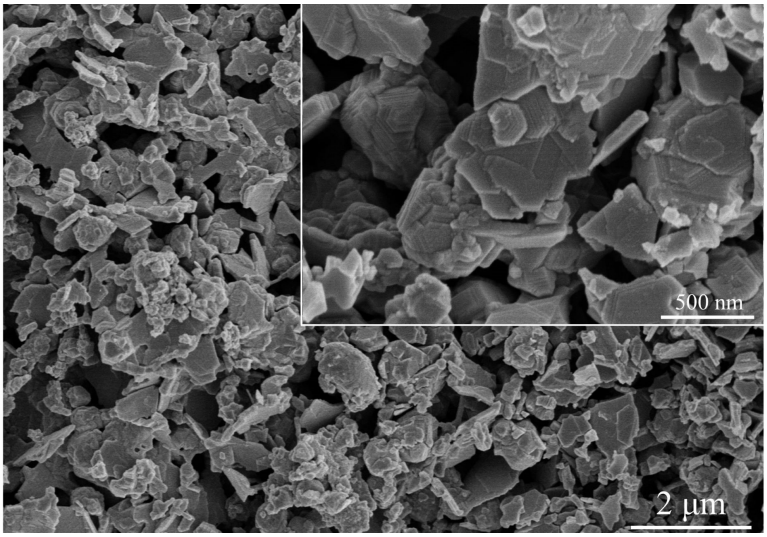

Fig. S6 SEM of NiFe.

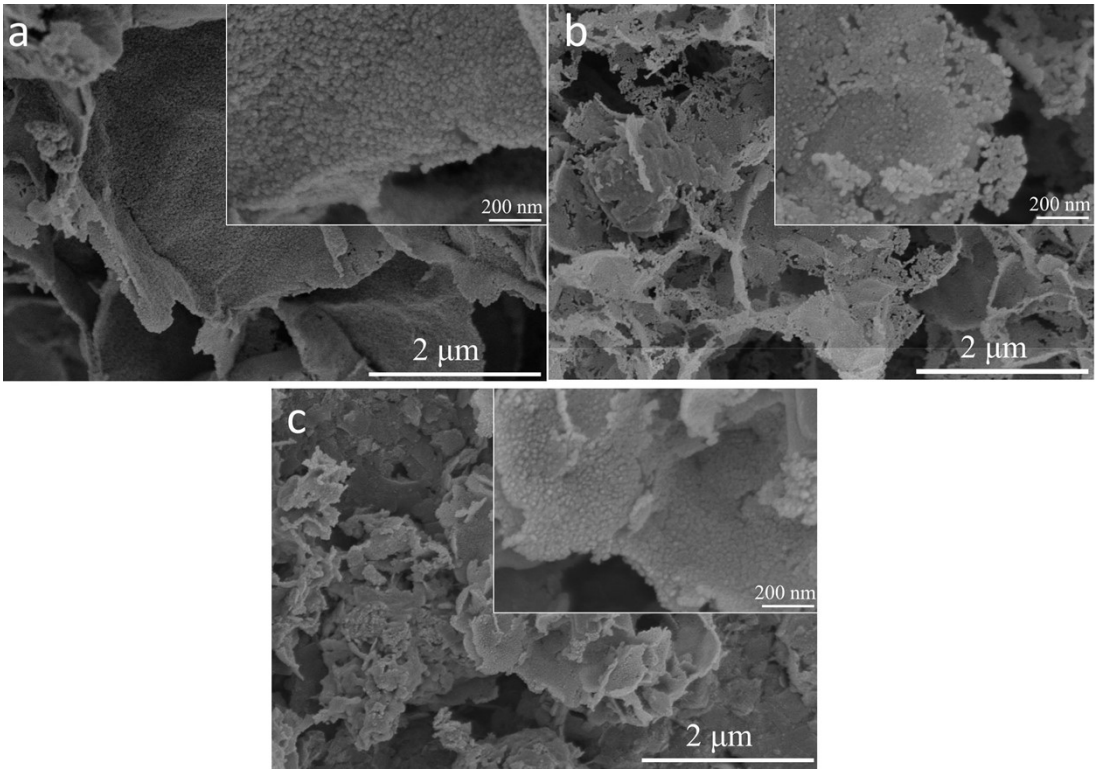

Fig. S7 SEM of (a) $Mo_{0.25}$-NiFe, (b) $Mo_{0.75}$-NiFe, (c) $Mo_{1.0}$-NiFe.

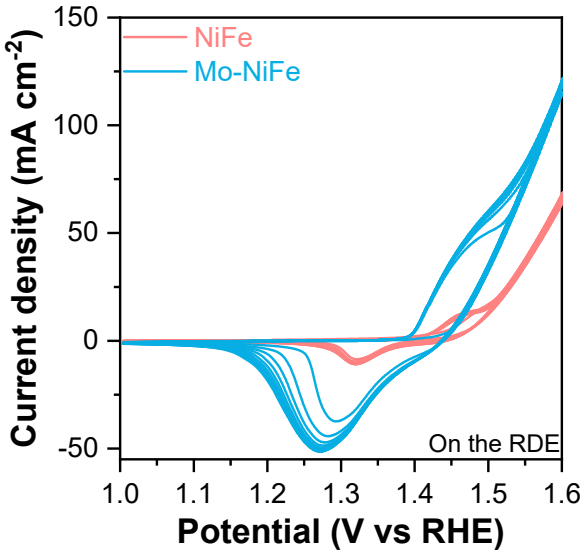

Fig. S8 CV curves of NiFe and Mo-NiFe on the RDE.

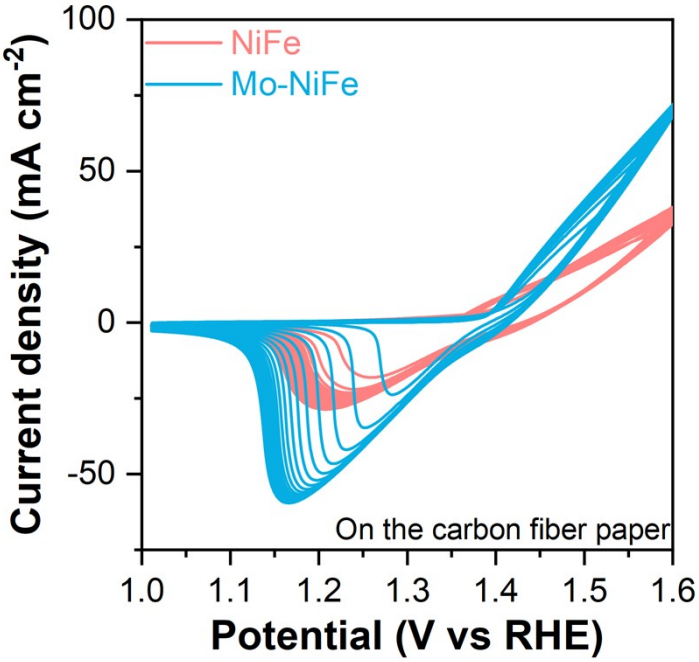

Fig. S9 CV curves of NiFe and Mo-NiFe spraying on carbon fiber paper (CFP).

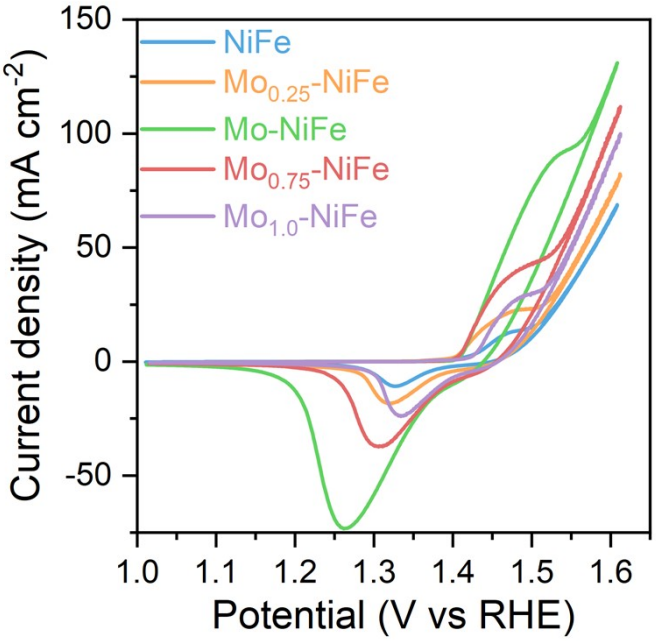

Fig. S10 CV of NiFe, $Mo_{0.25}$-NiFe, Mo-NiFe, $Mo_{0.75}$-NiFe and $Mo_{1.0}$-NiFe on the RDE.

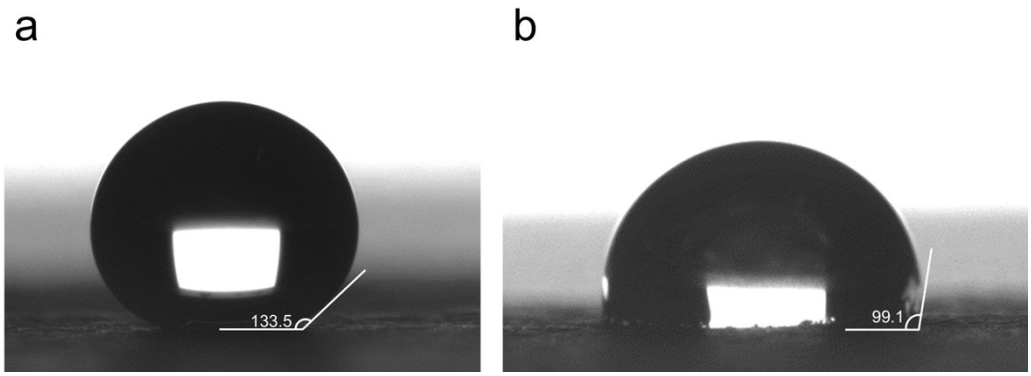

Fig. S11 Contact angle of Mo-NiFe/CFP (a) before and (b) after pre-oxidation.

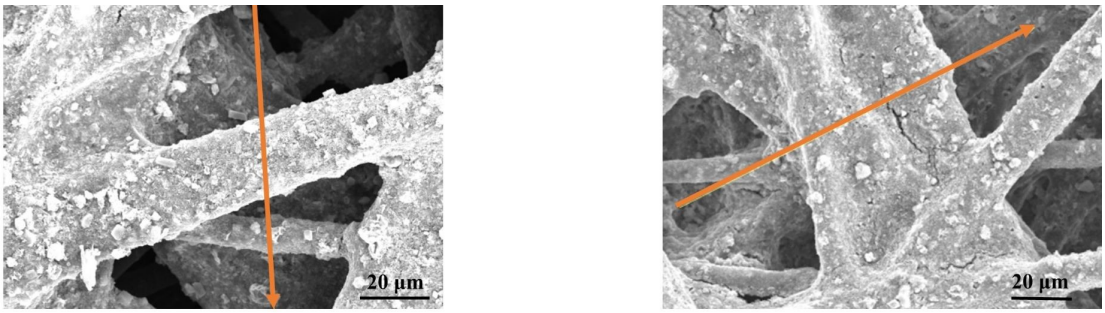

Element	wt%	at%	Abs.error [mass%]
Ni	37.4	44.92	2.73
Fe	17.21	21.73	1.17
Mo	45.38	33.35	2.92

After oxidation

Element	wt%	at%	Abs.error [mass%]
Ni	64.66	66.04	4.76
Fe	26.46	28.40	1.75
Mo	8.89	5.55	0.71

Fig. S12 Element content form SEM-EDX line scans of Mo-NiFe sprayed onto the carbon paper before and after oxidation.

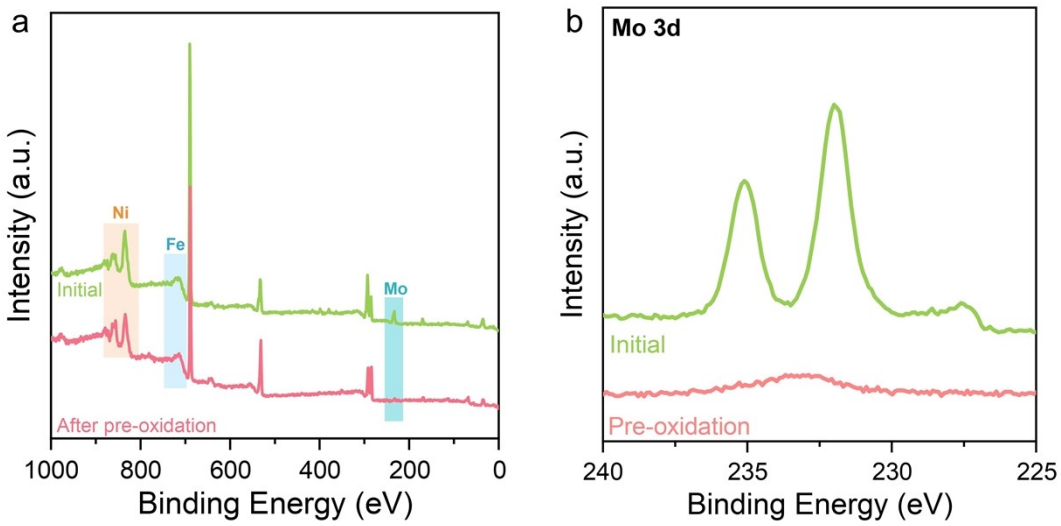

Fig. S13 XPS survey of Mo-NiFe/CFP before and after CV pre-oxidation.

The Mo ions can be oxidized to soluble MoO_4^{2-} in an alkaline electrolyte under the oxidation process ($Mo^{6+} + 8\ OH^- \rightarrow MoO_4^{2-} + 4\ H_2O$).

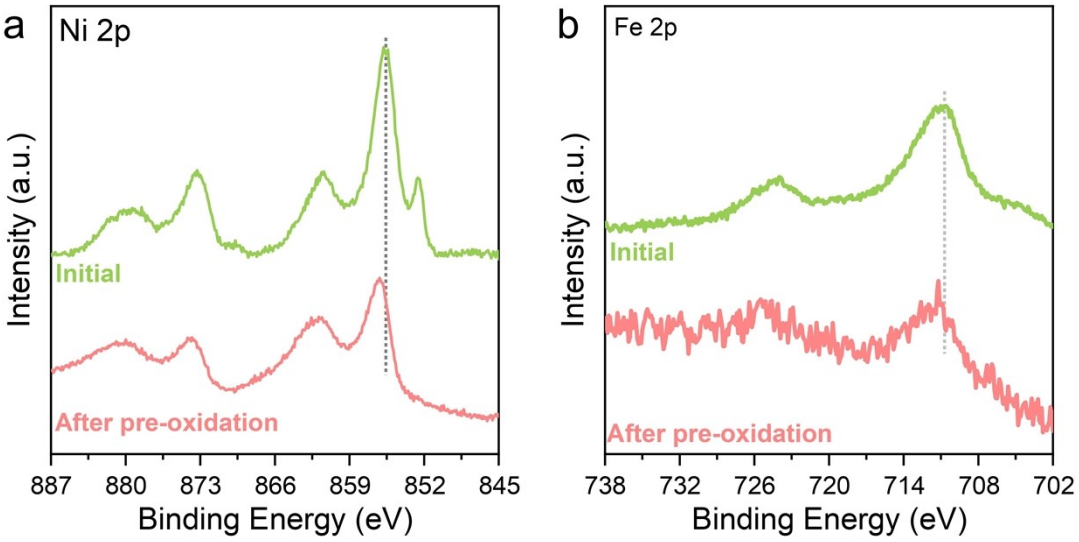

Fig. S14 (a) Ni 2p and (b) Fe 2p of Mo-NiFe before and after CV pre-oxidation.

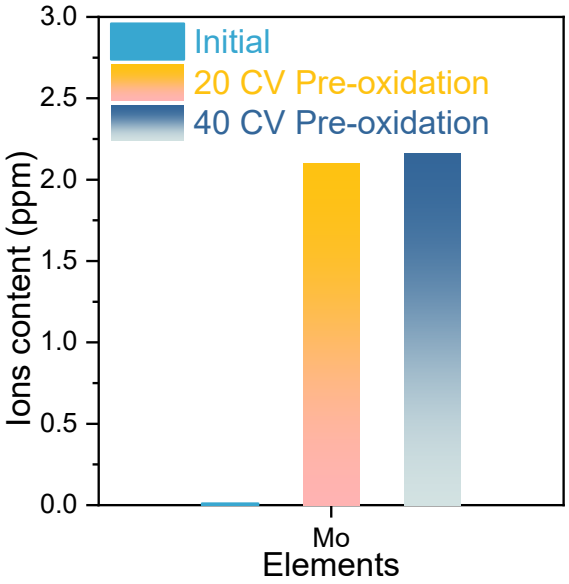

Fig. S15 Mo ion content in the solution of Mo-NiFe before and after CV pro-oxidation.

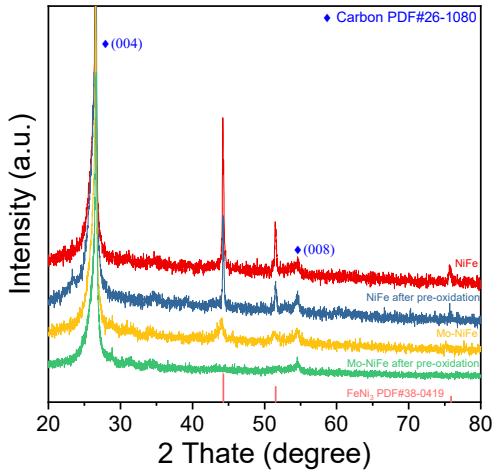

Fig. S16 XRD of NiFe and Mo-NiFe before and after CV pre-oxidation.

X-ray diffraction (XRD) analysis demonstrates the persistence of $FeNi_3$ phase in the NiFe sample post pre-oxidation, while no $FeNi_3$ diffraction peaks are detected in the Mo-doped NiFe sample. This distinct contrast confirms that Mo doping facilitates the complete phase transition of $FeNi_3$ during pre-oxidation, leading to the formation of new crystalline phases.

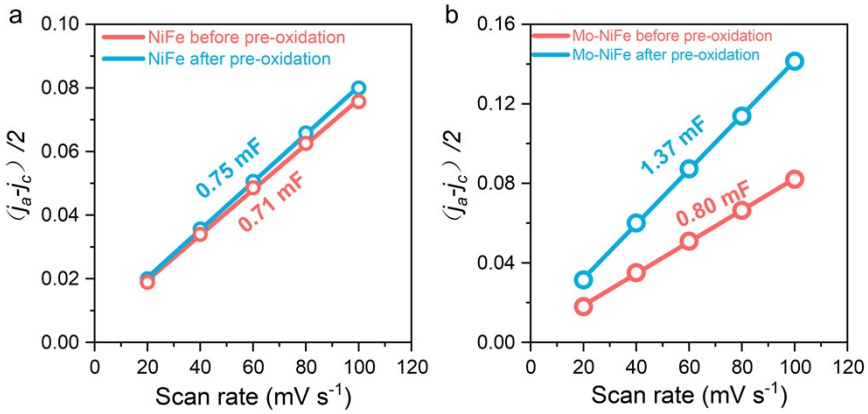

Fig. S17 The C_{dl} of (a) NiFe and (b) Mo-NiFe before and after pre-oxidation

The electrochemically active surface area (ECSA) of catalysts was determined based on the double-layer capacitance (C_{dl}) using cyclic voltammetry method. Electrochemical tests reveal that, compared to the NiFe, Mo-NiFe demonstrates a significant increase in ECSA after the pre-oxidation treatment, indicating bulk structure reconstruction of in Mo-NiFe.

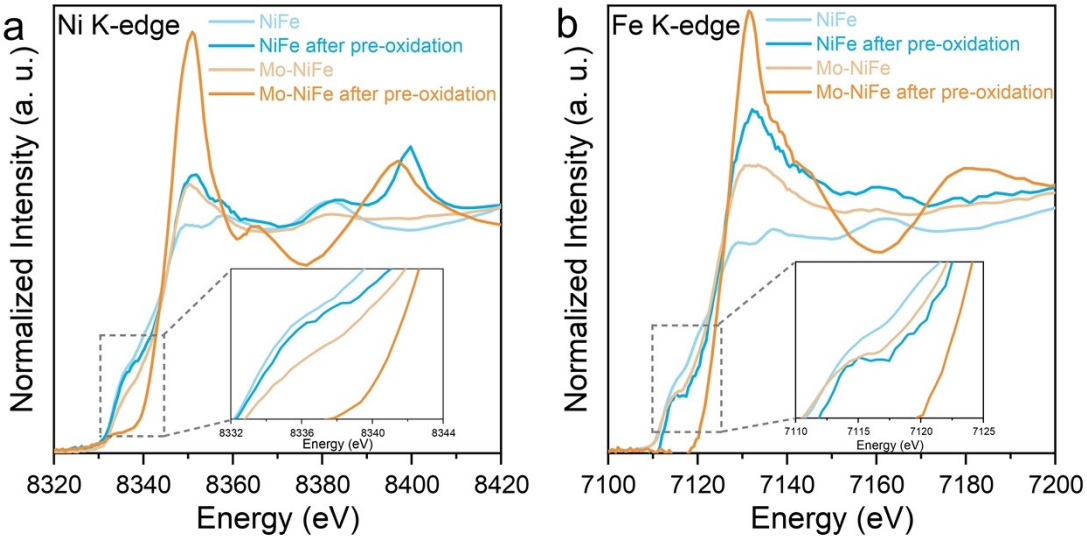

Fig. S18 XANES spectra of (a) Ni K-edge and (b) Fe K-edge for NiFe, Mo-NiFe before and after pre-oxidation.

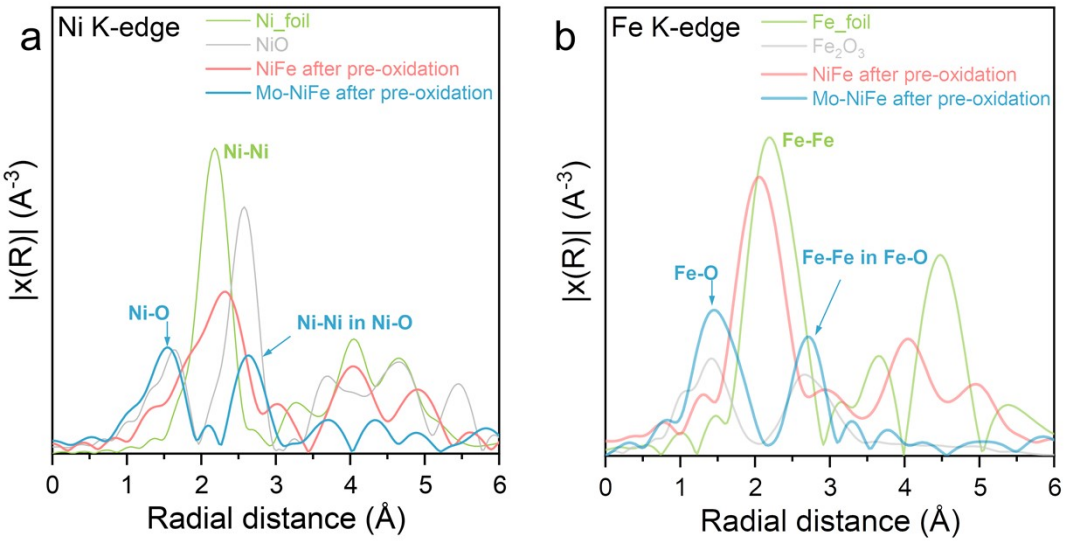

Fig. S19 EXAFS spectra of (a) Ni K-edge and (b) Fe K-edge for NiFe, Mo-NiFe after pre-oxidation.[9]

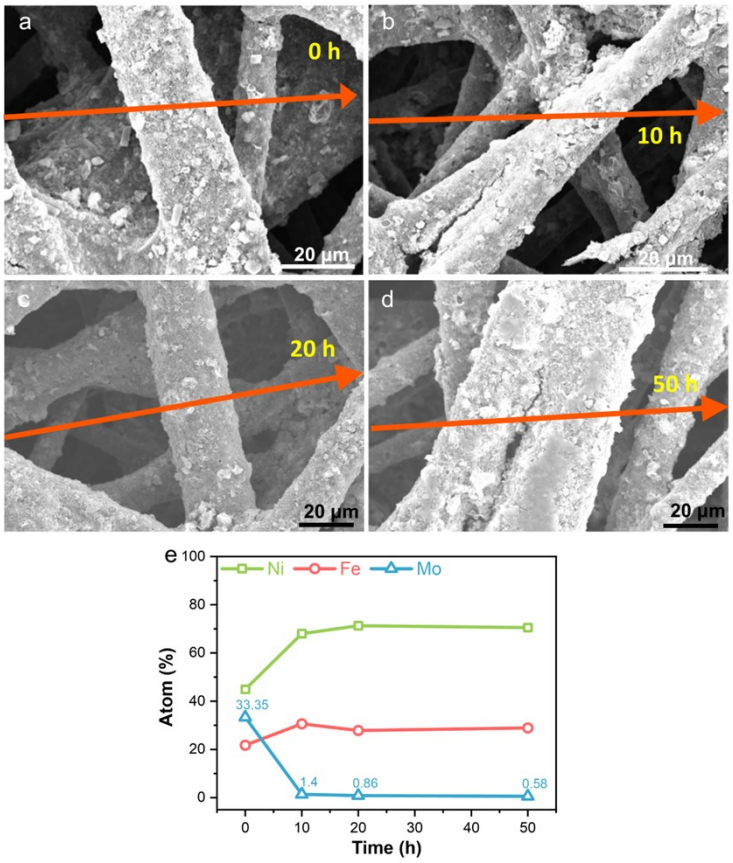

Fig. S20 (a-d) The SEM-EDX line scans of Mo-NiFe electrode at 1.55 V vs RHE under different times. (e) Mo, Ni, Fe content in the Mo-NiFe electrode from the EDX.

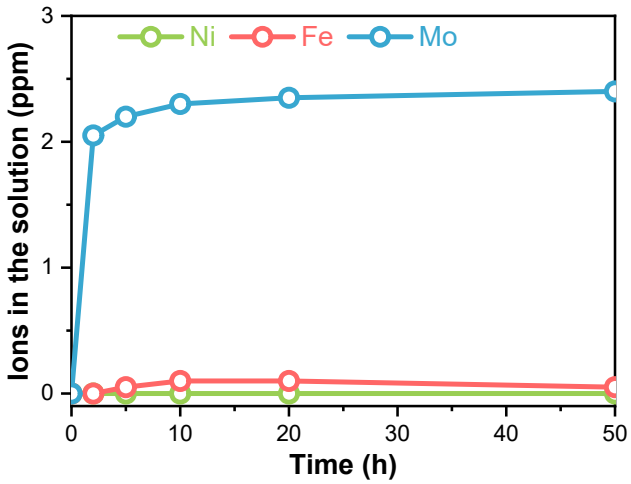

Fig. S21 Mo, Ni, Fe dissolved in electrolyte versus time from ICP for Mo-NiFe at 1.55 V vs RHE.

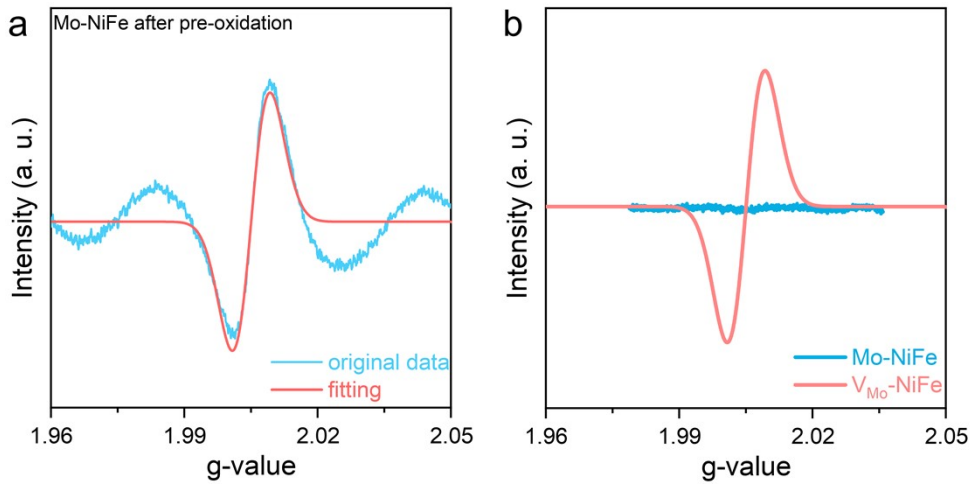

Fig. S22 EPR curves of the Mo-NiFe before and after pre-oxidation.

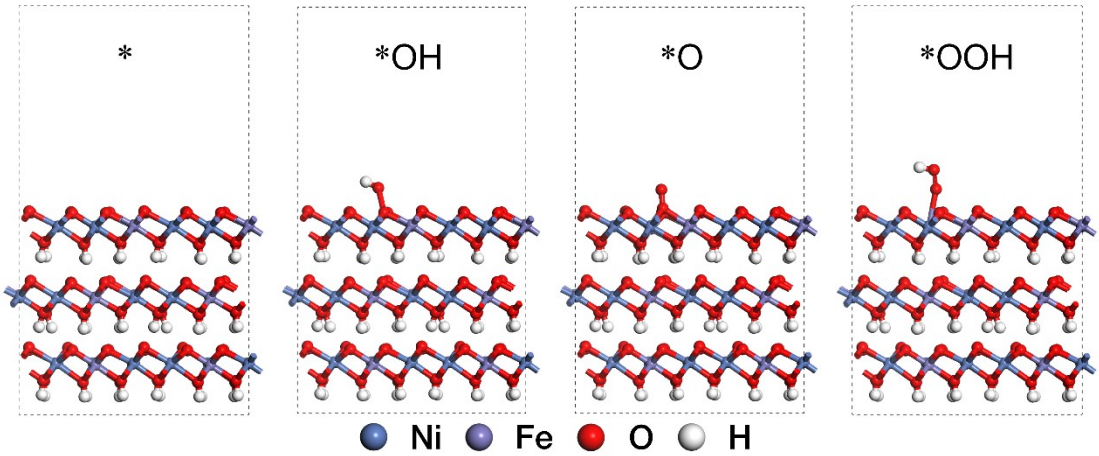

Fig. S23 Side views of the OER cycles for the $NiFeO_xH_y$ surface.

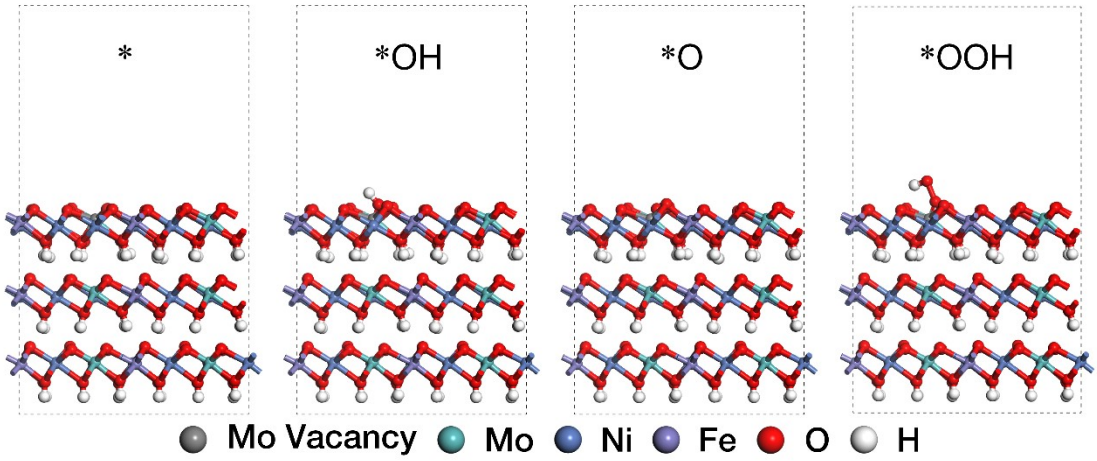

Fig. S24 Side views of the OER cycles for the V_{Mo}-$NiFeO_xH_y$ surface. The black atoms indicate cation vacancy.

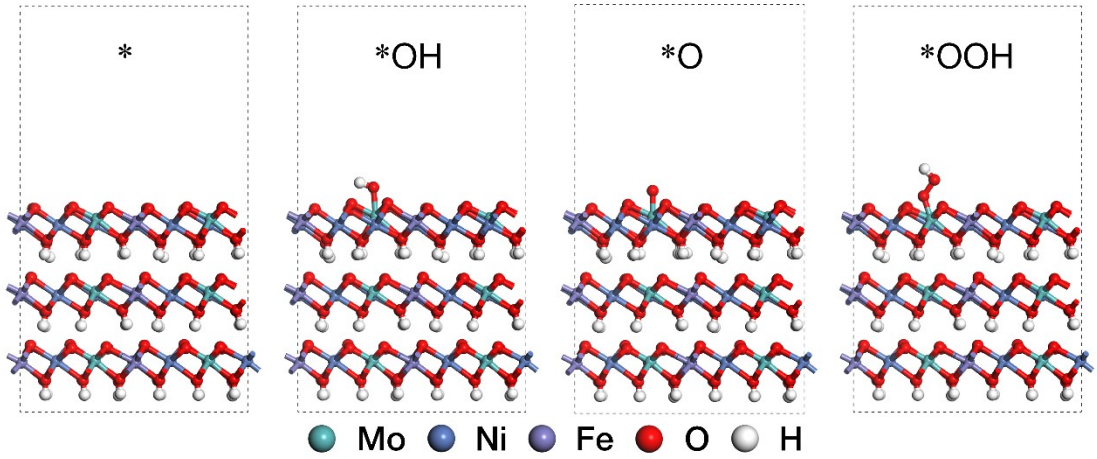

Fig. S25 Side views of the OER cycles for the Mo-$NiFeO_xH_y$ surface without cation vacancy.

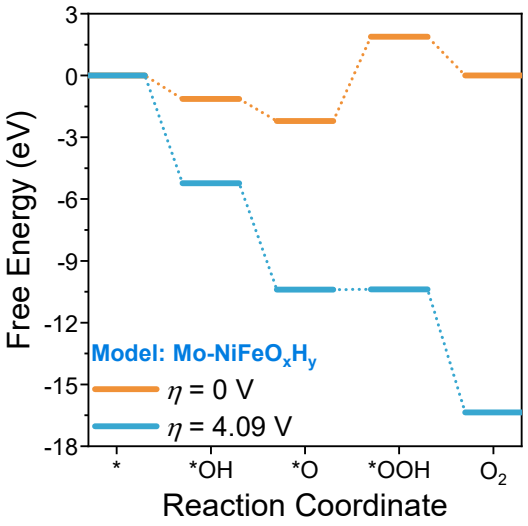

Fig. S26 Gibbs free energies of the four OER reaction steps of Mo-NiFeO$_x$H$_y$ model at different overpotential.

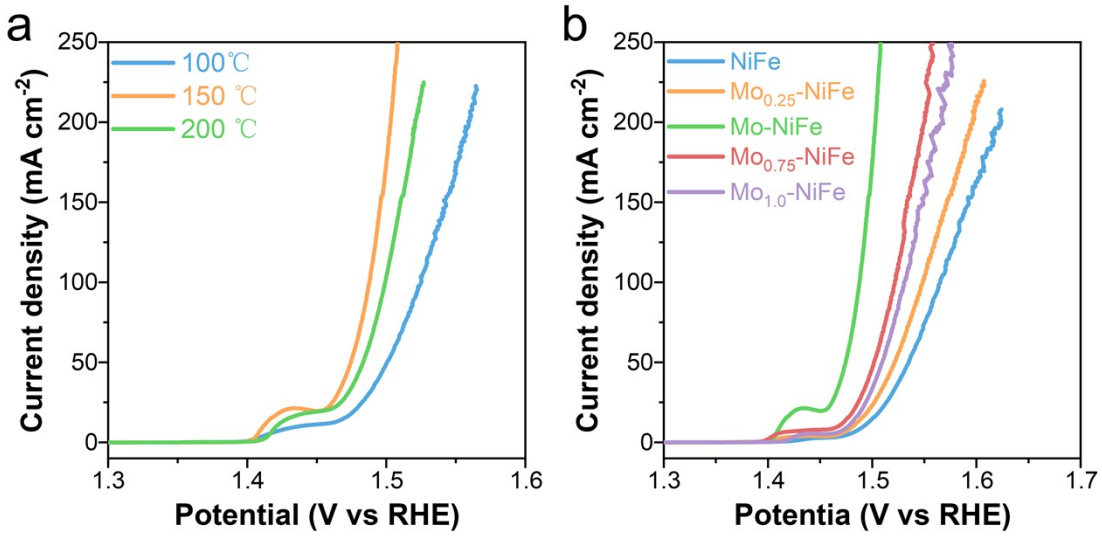

Fig. S27 (a) LSV of Mo-NiFe under different hydrothermal temperature, (b) LSV of NiFe, Mo$_{0.25}$-NiFe, Mo-NiFe, Mo$_{0.75}$-NiFe and Mo$_{1.0}$-NiFe on the RDE.

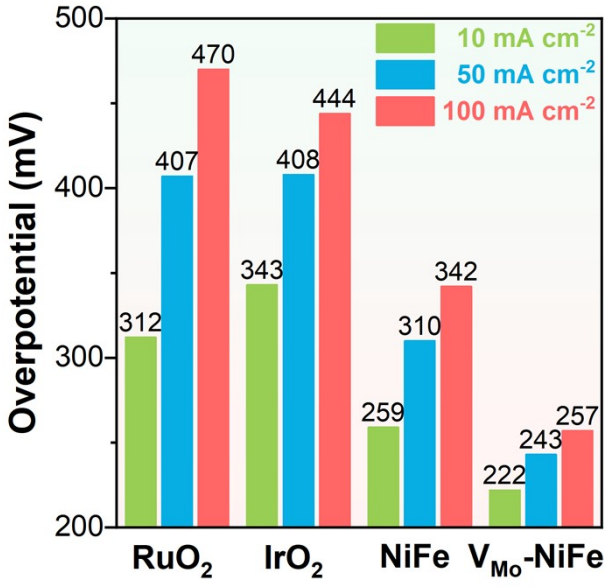

Fig. S28 The corresponding overpotential under different current density.

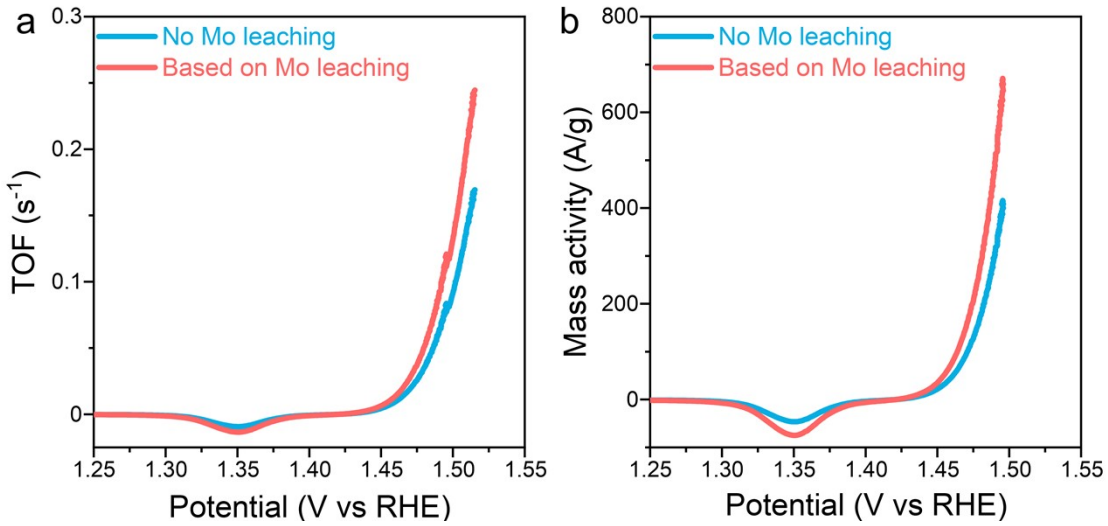

Fig. S29 The calculation of TOF and Mass activity curves considering the completive leaching of Mo ions.

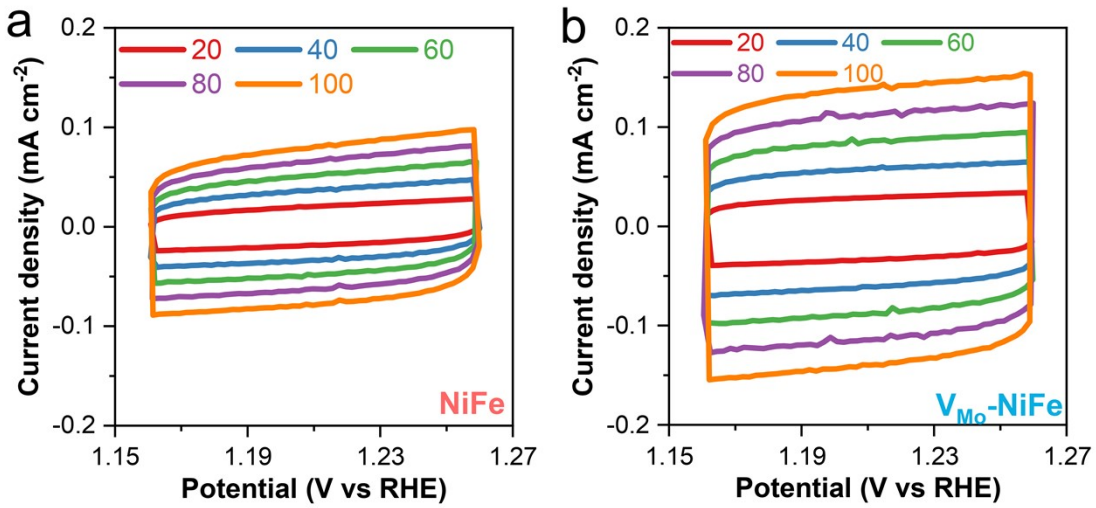

Fig. S30 CV curves with different scan rates of (a) NiFe, (b) V_{Mo}-NiFe.

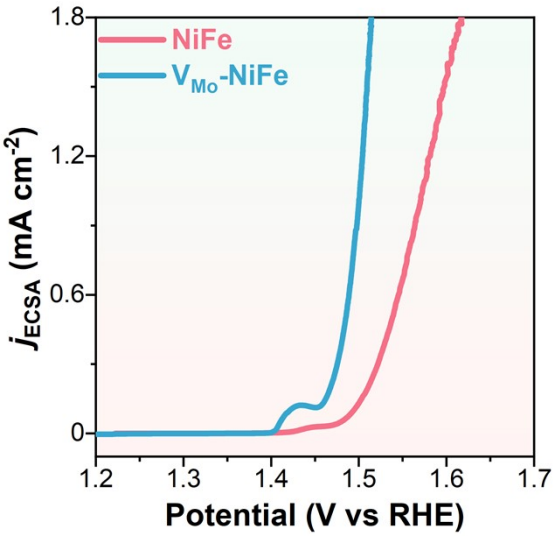

Fig. S31 The current density was normalized by the calculated ECSA.

Fig. S32 The single AEMWE cell test system.

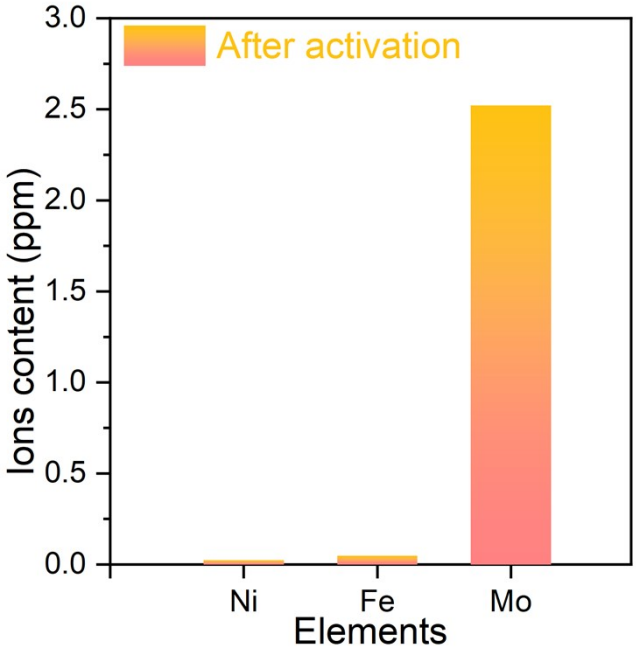

Fig. S33 Ni, Fe, Mo ions dissolved in electrolyte from ICP for Mo-NiFe as the anode of AEMWE after activation.

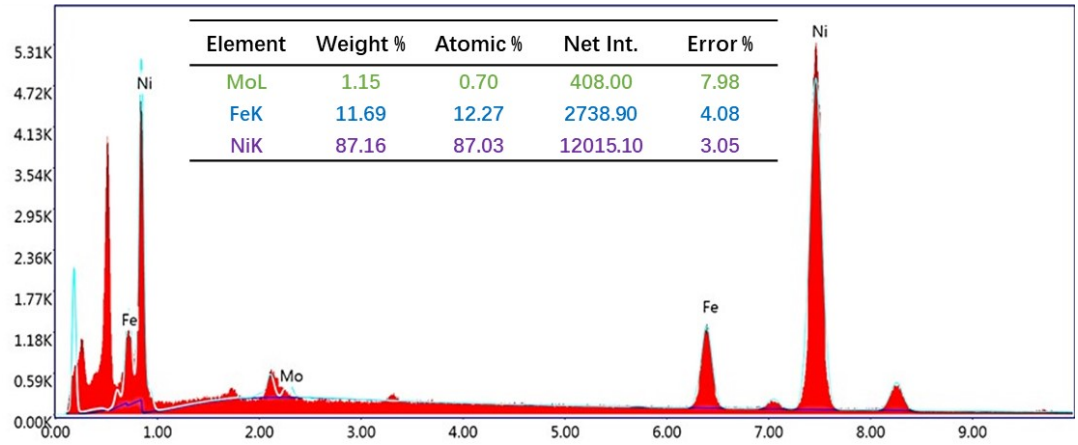

Fig. S34 Element content form SEM-EDX line scans of Mo-NiFe sprayed onto the Ni foam as the anode for AEMWE after activation. The high Ni content in EDX can partly attributed to the Ni-foam.

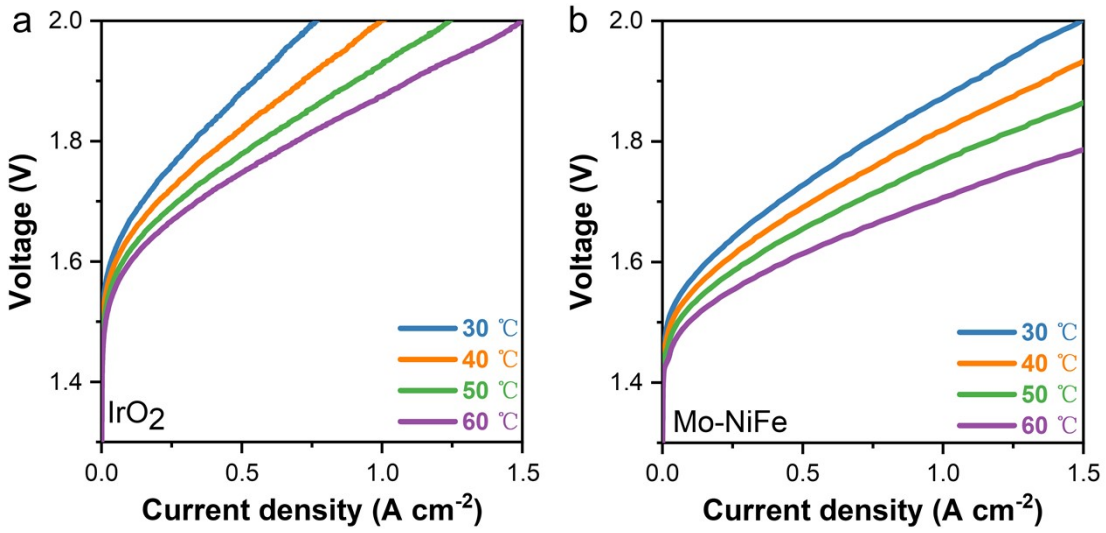

Fig. S35 The I-V curves of the AEMWE based on (a) IrO_2 and (b) Mo-NiFe at different temperatures.

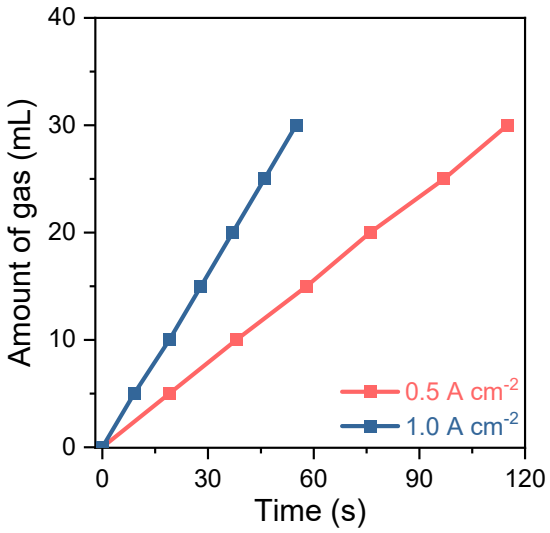

Fig. S36 The actually volume of H_2 gas under different current density.

The faradaic efficiency was determined by comparing the amounts of H_2 gas theoretically calculated and experimentally evolved.[10] The gas experimentally generated from the water splitting was collected by the water displacement method in an airtight vessel. The theoretically evolved oxygen was calculated using:

$$\text{Faradaic efficiency} = \frac{4 \times F \times N_{H_2}}{I \times t}$$

Where F is the Faraday constant (96 485 C mol^{-1}), N_{H_2} is the number of moles of H_2 that is calculated approximately by the ideal gas law, and I is the given value of current, t is the time (s) under constant applied current.

Fig. S37 Photo of Mo NiFe precursors (~24 g) prepared in large quantities.

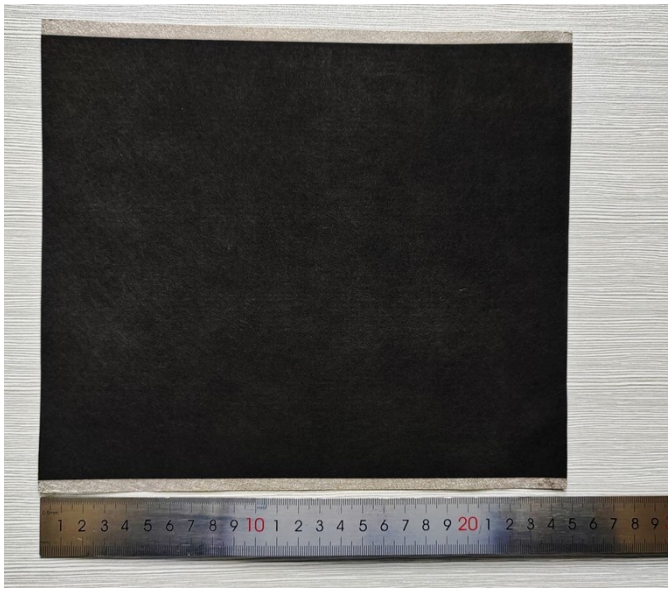

Fig. S38 The 25 × 25 cm electrode for AEMWE stack using automatic spraying.

Table S1 ICP-MS results for Ni, Fe and Mo contents in NiFe and Mo-NiFe.

Samples	Ni (wt%)	Fe (wt%)	Mo (wt%)
NiFe	69.87%	29.91%	/
Mo-NiFe	35.09%	16.56%	37.97%

Table S2 Comparison of the OER activity of vacancy modified catalysts.

Catalyst		Vacancy	Overpotential	Loading (mg cm^{-2})	Reference
Anion vacancy	CoFe LDH	O	266 mV@10 mA cm^{-2}	0.5 on RDE	[11]
	NiFe LDH	O	226 mV@10 mA cm^{-2}	--	[12]
	$Bi_{0.15}Sr_{0.85}Co_{1-x}Fe_xO_{3-\delta}$	O	~3330 mV@10 mA cm^{-2}	0.255 on RDE	[13]
	NiFe-S-Vs/NF	S	252 mV@100 mA cm^{-2}	Ni foam self-support	[14]
	CoFeLDH-O_v	O	220 mV@30 mA cm^{-2}	Ni foam self-support	[15]
Cation vacancy	CoOOH-W_D-Co_V	Co	298.5 mV@50 mA cm^{-2}	--	[16]
	$Ni^{vac}Fe^{vac}$-LDH	Zn/Al	230 mV@10 mA cm^{-2}	0.1 (dropped onto carbon paper)	[17]
	Co, V_M-NiFe OOH	Mo	255 mV@100 mA cm^{-2}	Ni foam self-support	[18]
	NiCoAlO-P	Co	300 mV@100 mA cm^{-2}	0.3 on RDE	[19]
	CoOOH	Co	298.5 mV@50 mA cm^{-2}	Ni foam self-support	[20]

Reference:

[1] S.J. Clark, M.D. Segall, C.J. Pickard, P.J. Hasnip, M.I.J. Probert, K. Refson, M.C. Payne, First principles methods using CASTEP, Z. Krist. - Cryst. Mater. 220 (2005) 567–570. https://doi.org/10.1524/zkri.220.5.567.65075.

[2] S.L. Dudarev, G.A. Botton, S.Y. Savrasov, C.J. Humphreys, A.P. Sutton, Electron-energy-loss spectra and the structural stability of nickel oxide: an LSDA+U study, Phys. Rev. B 57 (1998) 1505–1509. https://doi.org/10.1103/PhysRevB.57.1505.

[3] Y. Peng, H. Hajiyani, R. Pentcheva, Influence of Fe and Ni Doping on the OER Performance at the Co_3O_4(001) Surface: Insights from DFT+*U* Calculations, ACS Catal. 11 (2021) 5601–5613. https://doi.org/10.1021/acscatal.1c00214.

[4] J. Li, J. Song, B.-Y. Huang, G. Liang, W. Liang, G. Huang, Y. Qi Jin, H. Zhang, F. Xie, J. Chen, N. Wang, Y. Jin, X.-B. Li, H. Meng, Enhancing the oxygen evolution reaction performance of NiFeOOH electrocatalyst for Zn-air battery by N-doping, J. Catal. 389 (2020) 375–381. https://doi.org/10.1016/j.jcat.2020.06.022.

[5] H.J. Monkhorst, J.D. Pack, Special points for brillouin-zone integrations, Phys. Rev. B 13 (1976) 5188–5192. https://doi.org/10.1103/PhysRevB.13.5188.

[6] J. Rossmeisl, Z.-W. Qu, H. Zhu, G.-J. Kroes, J.K. Nørskov, Electrolysis of water on oxide surfaces, J. Electroanal. Chem. 607 (2007) 83–89. https://doi.org/10.1016/j.jelechem.2006.11.008.

[7] D. Friebel, M.W. Louie, M. Bajdich, K.E. Sanwald, Y. Cai, A.M. Wise, M.-J. Cheng, D. Sokaras, T.-C. Weng, R. Alonso-Mori, R.C. Davis, J.R. Bargar, J.K. Nørskov, A. Nilsson, A.T. Bell, Identification of highly active Fe sites in (Ni,Fe)OOH for electrocatalytic water splitting, J. Am. Chem. Soc. 137 (2015) 1305–1313. https://doi.org/10.1021/ja511559d.

[8] J.K. Nørskov, J. Rossmeisl, A. Logadottir, L. Lindqvist, J.R. Kitchin, T. Bligaard, H. Jónsson, Origin of the overpotential for oxygen reduction at a fuel-cell cathode, J. Phys. Chem. B 108 (2004) 17886–17892. https://doi.org/10.1021/jp047349j.

[9] Y. Lin, J. Fang, W. Wang, Q. Wen, D. Huang, D. Ding, Z. Li, Y. Liu, Y. Shen, T. Zhai, Operando Reconstructed Molecule Fence to Stabilize NiFe-Based Oxygen Evolution Catalysts, Adv. Energy Mater. 13 (2023) 2300604. https://doi.org/10.1002/aenm.202300604.

[10] Z. Ahmed, Krishankant, R. Rai, R. Kumar, T. Maruyama, C. Bera, V. Bagchi, Unraveling a Graphene Exfoliation Technique Analogy in the Making of Ultrathin Nickel–Iron Oxyhydroxides@Nickel Foam to Promote the OER, ACS Appl. Mater. Interfaces 13 (2021) 55281–55291. https://doi.org/10.1021/acsami.1c19536.

[11] S. Das, B. Wang, Y. Cao, M. Rae Cho, Y. Jae Shin, S. Mo Yang, L. Wang, M. Kim, S.V. Kalinin, L.-Q. Chen, T.W. Noh, Controlled manipulation of oxygen vacancies using nanoscale flexoelectricity, Nat. Commun. 8 (2017) 615. https://doi.org/10.1038/s41467-017-00710-5.

[12] J. Hu, D. Jiang, Z. Weng, Y. Pan, Z. Li, H. Du, Y. Yuan, A universal electrochemical activation enabling lattice oxygen activation in nickel-based catalyst for efficient water oxidation, Chem. Eng. J. 430 (2022) 132736.

https://doi.org/10.1016/j.cej.2021.132736.

[13] J. Li, F. Yang, Y. Du, M. Jiang, X. Cai, Q. Hu, J. Zhang, The critical role of A, B-site cations and oxygen vacancies on the OER electrocatalytic performances of $Bi_{0.15}Sr_{0.85}Co_{1-x}Fe_xO_{3-\delta}$ ($0.2 \leq x \leq 1$) perovskites in alkaline media, Chem. Eng. J. 451 (2023) 138646. https://doi.org/10.1016/j.cej.2022.138646.

[14] L. He, N. Wang, M. Xiang, L. Zhong, S. Komarneni, W. Hu, S-vacancy-rich NiFe-S nanosheets based on a fully electrochemical strategy for large-scale and quasi-industrial OER catalysts, Appl. Catal. B: Environ. Energy 345 (2024) 123686. https://doi.org/10.1016/j.apcatb.2023.123686.

[15] Krishankant, Aashi, A. Jain, J. Sharma, R. Rani, C. Bera, V. Bagchi, Unfolding the Electrocatalytic Efficiency of Ultrastable CoFeLDH Nanorods by Creating Oxygen Vacancies for OER, ACS Appl. Energy Mater. 7 (2024) 1027–1036. https://doi.org/10.1021/acsaem.3c02468.

[16] Y. Dou, D. Yuan, L. Yu, W. Zhang, L. Zhang, K. Fan, M. Al-Mamun, P. Liu, C.-T. He, H. Zhao, Interpolation between W Dopant and Co Vacancy in CoOOH for Enhanced Oxygen Evolution Catalysis, Adv. Mater. 34 (2022) 2104667. https://doi.org/10.1002/adma.202104667.

[17] L. Peng, N. Yang, Y. Yang, Q. Wang, X. Xie, D. Sun-Waterhouse, L. Shang, T. Zhang, G.I.N. Waterhouse, Atomic Cation-Vacancy Engineering of NiFe-Layered Double Hydroxides for Improved Activity and Stability towards the Oxygen Evolution Reaction, Angew. Chem. Int. Ed. 60 (2021) 24612–24619. https://doi.org/10.1002/anie.202109938.

[18] Y. Zhao, Q. Wen, D. Huang, C. Jiao, Y. Liu, Y. Liu, J. Fang, M. Sun, L. Yu, Operando Reconstruction toward Dual-Cation-Defects Co-Containing NiFe Oxyhydroxide for Ultralow Energy Consumption Industrial Water Splitting Electrolyzer, Adv. Energy Mater. 13 (2023) 2203595. https://doi.org/10.1002/aenm.202203595.

[19] J. Zheng, X. Peng, Z. Xu, J. Gong, Z. Wang, Cationic Defect Engineering in Spinel $NiCo_2O_4$ for Enhanced Electrocatalytic Oxygen Evolution, ACS Catal. 12 (2022) 10245–10254. https://doi.org/10.1021/acscatal.2c01825.

[20] Y. Dou, D. Yuan, L. Yu, W. Zhang, L. Zhang, K. Fan, M. Al-Mamun, P. Liu, C.-T. He, H. Zhao, Interpolation between W Dopant and Co Vacancy in CoOOH for Enhanced Oxygen Evolution Catalysis, Adv. Mater. 34 (2022) 2104667. https://doi.org/10.1002/adma.202104667.